U.S. DEPARTMENT OF ENERGY

PNNL-21156

Prepared for the U.S. Department of Energy
under Contract DE-AC05-76RL01830

Soret Effect Study on High-Pressure CO_2-Water Solutions Using UV-Raman Spectroscopy and a Concentric-Tube Optical Cell

CF Windisch Jr.
BP McGrail
GD Maupin

January 2012

Pacific Northwest
NATIONAL LABORATORY

Proudly Operated by Battelle *Since 1965*

PACIFIC NORTHWEST NATIONAL LABORATORY
operated by
BATTELLE
for the
UNITED STATES DEPARTMENT OF ENERGY
under Contract DE-AC05-76RL01830

Printed in the United States of America

Available to DOE and DOE contractors from the
Office of Scientific and Technical Information,
P.O. Box 62, Oak Ridge, TN 37831-0062;
ph: (865) 576-8401
fax: (865) 576-5728
email: reports@adonis.osti.gov

Available to the public from the National Technical Information Service
5301 Shawnee Rd., Alexandria, VA 22312
ph: (800) 553-NTIS (6847)
email: orders@ntis.gov <http://www.ntis.gov/about/form.aspx>
Online ordering: http://www.ntis.gov

This document was printed on recycled paper.
(8/2010)

PNNL-21156

Soret Effect Study on High-Pressure CO_2-Water Solutions Using UV-Raman Spectroscopy and a Concentric-Tube Optical Cell

CF Windisch Jr.
BP McGrail
GD Maupin

January 2012

Prepared for
the U.S. Department of Energy
under Contract DE-AC05-76RL01830

Pacific Northwest National Laboratory
Richland, Washington 99352

Abstract

Spatially resolved deep-UV Raman spectroscopy was applied to solutions of CO_2 and H_2O (or D_2O), which were subject to a temperature gradient in a thermally regulated high-pressure concentric-tube Raman cell in an attempt to measure a Soret effect in the vicinity of the critical point of CO_2. Although Raman spectra of solutions of CO_2 dissolved in D_2O at 10 MPa and temperatures near the critical point of CO_2 had adequate signal-to-noise and spatial resolution to observe a Soret effect with a Soret coefficient with magnitude of $|S_T| > 0.03$, no evidence for an effect of this size was obtained for applied temperature gradients up to 19^oC. The presence of 1 M NaCl did not make a difference. In contrast, the concentration of CO_2 dissolved in H_2O was shown to vary significantly across the temperature gradient when excess CO_2 was present, but the results could be explained simply by the variation in CO_2 solubility over the temperature range and not to kinetic factors. For mixtures of D_2O dissolved in scCO_2 at 10 MPa and temperatures close to the critical point of CO_2, the Raman peaks for H_2O were too weak to measure with confidence even at the limit of D_2O solubility.

Acknowledgments

This work was supported by the U.S. Department of Energy (DOE), Office of Fossil Energy. The Pacific Northwest National Laboratory (PNNL) is operated by Battelle for the DOE under Contract DE-AC05-76RL01830.

Acronyms and Abbreviations

BBO	beta barium borate
cm	centimeter
CO_2	carbon dioxide
D_2O	heavy water
H_2O	water
mm	millimeter
MPa	megapascals
NaCl	sodium chloride
$scCO_2$	supercritical carbon dioxide
μm	micron
UV	ultraviolet
ZERT	Zero Emissions Research and Technology

Contents

Abstract iii
Acknowledgments iv
Acronyms and Abbreviations v
1.0 Introduction 1
1.1 Overall program objective 1
1.2 Summary of ZERT I results 2
1.3 Justification and description of approach for ZERT II 2
2.0 Experimental Procedure 4
2.1 Concentric-tube Raman cell design 4
2.2 UV-Raman spectrometer 7
2.3 Typical experiment and variables 8
3.0 Results 11
3.1 Assessment of Raman cell 11
3.1.1 Position of the microscope objective vs. focal point of the measurement 11
3.1.2 Estimate of sampling volume 12
3.2 Raman spectra 12
3.2.1 Experiments on D_2O containing CO_2 below saturation 12
3.2.2 Experiments on D_2O + 1 M NaCl containing CO_2 below saturation 17
3.2.3 Varied pressure study 18
3.2.4 H_2O containing CO_2 at saturation 19
3.2.5 $scCO_2$ containing D_2O at saturation 20
4.0 Discussion 22
4.1 Solutions of CO_2 in D_2O with CO_2 below saturation 22
4.2 Solutions of H_2O saturated with CO_2 23
4.2 Concentration calibration plots 25
5.0 References 27

Figures

Figure 1. Simplified schematic of concentric-tube Raman cell. 3

Figure 2. Concentric-tube Raman cell in cross-section showing thicknesses of the tubes and the annuli.. 4

Figure 3. Comparisons of the UV-Raman spectra of H_2O and D_2O, at room temperature and atmospheric pressure, with the principal peaks of CO_2 (Fermi dyad) also shown..... 5

Figure 4. Schematic of the concentric-tube Raman cell within its assembly..... 6

Figure 5. Photograph of the concentric-tube Raman cell assembly positioned under the UV-Raman spectrometer microscope objective..... 6

Figure 6. Images of the reflected laser light from the stainless steel tube in the center of the Raman cell, (a) with the incident light focus on the bare steel, (b) with the incident light focused on the steel with a high-temperature air-formed film (held at 600°C overnight), and (c) with the incident light focused on a “blued” steel surface. 7

Figure 7. Photograph of the concentric-tube Raman cell assembly, UV-Raman spectrometer, and ancillary equipment..... 8

Figure 8. Total Raman scattering signal strength (from both CO_2 and D_2O) as a function of the position of the objective (z value). In relationship to position within the annulus, z = 0 μm corresponds to the inside surface of the sapphire tube, whereas z = 2000 μm is near the outside surface of the stainless steel tube. The photographs are white-light images at these two positions. Circles around each point indicate the approximate sampling volumes. 11

Figure 9. UV-Raman spectra as a function of position within the annulus (in terms of the microscope position, z), with $X(CO_2)$ = 0.0054, T(inside) = 12°C and T(outside) = 30°C. Higher temperature is outside. The spectra were acquired in the direction of increasing z. CO_2 is a liquid under these conditions..... 13

Figure 10. UV-Raman spectra as a function of position within the annulus (in terms of the microscope position, z), with $X(CO_2)$ = 0.0027, T(inside) = 45°C and T(outside) = 33°C. The higher temperature is inside. The spectra were acquired in the direction of increasing z. CO_2 is supercritical under these conditions. 14

Figure 11. CO_2/D_2O peak intensity ratio calculated from the Raman spectra as a function of position for $X(CO_2)$ = 0.0014 and 0.0027, with different temperature gradients and direction of scan. 15

Figure 12. CO_2/D_2O peak intensity ratio calculated from the Raman spectra as a function of position for $X(CO_2)$ = 0.0054, T(outside) = 30°C and T(inside) = 12°C, in both increasing- and decreasing-z directions..... 15

Figure 13. CO_2/D_2O peak intensity ratio calculated from the Raman spectra as a function of position for $X(CO_2)$ = 0.0027 with T(outside) = T(inside) at 32°C and 40°C. Spectra were collected in the direction of increasing z. 16

Figure 14. UV-Raman spectra at two positions within the annulus with $X(CO_2)$ = 0.0027 and T(outside) = T(0 μm) = 45°C and with varying T(inside). Spectra are shown for T(inside) = T(2000 μm) = 45°C, 40°C, 35°C, 30°C, 25°C, and 20°C..... 17

Figure 15. CO_2/D_2O peak intensity ratio, for solutions containing 1 M NaCl, as a function of position with $X(CO_2)$ = 0.0044, and various temperature gradients. Open symbols are ratios for the same experiments as the corresponding closed symbols, but were calculated using integrated intensities from curve fitting results..... 18

Figure 16. CO_2/D_2O peak intensity ratio, for solution with $X(CO_2) = 0.0027$ and T(inside) = T(outside) = 40°C, as a function of cell pressure. 19

Figure 17. UV-Raman spectra as a function of position within the annulus (in terms of the microscope position, z), for H_2O saturated with CO_2, i.e., $X(CO_2) \sim 0.028$. T(inside) = 11°C and T(outside) = 15°C. Spectra were acquired in the direction of increasing z. Spectral intensities are normalized with respect to the H_2O peak at 1640 cm-1. 19

Figure 18. $CO_2/(CO_2 + D_2O)$ peak intensity fraction calculated from the Raman spectra as a function of position, for H_2O saturated with CO_2, i.e., $X(CO_2) \sim 0.028$. Results are shown for measurements made with both increasing and decreasing z. Linear regression in the absence of the two low-z points is shown. 20

Figure 19. UV-Raman spectra as a function of position within the annulus for solutions of $scCO_2$ containing D_2O at saturation (i.e., $X(D_2O) \sim 0.003$). T(inside) = 32°C and T(outside) = 40°C. 21

Figure 20. Re-plot of Figure 11 showing straight lines fitted by eye to limits of error bars of the data for $X(CO_2) = 0.0014$. 23

Figure 21. Re-plot of Figure 17 noting intensity values at z = 0 μm and z = 2000 μm that were used to compare the observed variation with temperature to predictions based on solubility. 24

Figure 22. Plot of the fraction of total Raman scattering intensity attributed to CO_2 versus the mole fraction of CO_2 in the mixture as calculated from the quantities used in preparation. 25

Figure 23. Plot of the fraction of total Raman scattering intensity attributed to CO_2 versus the mole fraction of CO_2 in the mixture as calculated from the quantities used in preparation. 26

1.0 Introduction

1.1 Overall program objective

Considerable work on flow processes in CO_2-water[1] systems has been done in geothermal reservoir engineering. However, significant uncertainties remain with respect to mixing processes that occur in supercritical CO_2-water systems, especially in porous media. For the case where supercritical CO_2 is injected into a deep saline formation, the important processes to be considered include the following: (1) forced convective flow around the injection well, (2) dissolution rate of CO_2 into the brine, and (3) heat of solution as CO_2 dissolves into the formation brine.

As CO_2 dissolves into water, the negative heat of solution consumes approximately 17 kJ/mol at typical reservoir conditions (Bastelli 1997; White 2002). Also, pipeline supply of CO_2 will result in cold CO_2 reaching the wellhead. Reservoir calculations suggest that temperature gradients on the order of 5 to 10°C cm^{-1} can easily be generated as a result. A temperature gradient induces coupled feedback effects on the rate of convective mixing in two ways: (1) through changes in physical properties (density, viscosity, surface tension) and (2) nonlinear thermal diffusion or Soret effects (Kempers 2001; Nejad 2001). The Soret effect is the tendency of a mixture of two or more components to separate under the influence of a temperature gradient. The effect is quantified by the Soret coefficient, S_T, which is derived by considering Fick's law under conditions where the flux results from a combination of thermal and concentration gradients.

Empirical descriptions treat the mass flux associated with a thermal gradient, $\mathbf{j_T}$, as

$$\mathbf{j_T} = -D_T c \nabla T \qquad (1)$$

where D_T is the thermal diffusion coefficient of the diffusing species in the solution, c is the concentration and T is the temperature. It is considered a separate process from the mass flux associated with a concentration gradient, $\mathbf{j_c}$, which is given by

$$\mathbf{j_c} = -D \nabla c \qquad (2)$$

where D is the ordinary (mass) diffusion coefficient. Under steady-state conditions, $\mathbf{j_T} = -\mathbf{j_c}$, yielding (Duhr 2006):

$$\nabla c = -c S_T \nabla T \qquad (3)$$

where $S_T = D_T/D$ and is called the Soret coefficient. In concentrated mixtures, S_T is also a function of the solute concentration and can even change sign (Kolodner et al. 1988; Slavtchev et al. 1999).

[1] CO_2-water is the general term for the solutions studied here. Both isotopic forms of water, H_2O and D_2O, were used for reasons discussed in the text. For specific experiments, the form of water is called out in the notation, e.g., CO_2-D_2O.

Because of rapid changes in thermochemical properties near critical points (Zhang 2002) and based on independent measurements of supercritical CO_2 fluids (Swinney 1968), Soret effects have been predicted to be strong in near-critical liquids (Kempers 2001). The primary objective of the Fundamental Studies Task of Zero Emissions Research and Technology (ZERT) was to use laser Raman spectroscopy to study the Soret effect in CO_2-water mixtures across a temperature gradient near the critical point of CO_2. The proposed approach is based on other optical studies of the phenomenon (Xu 2003; Duhr 2006; Ning 2006; Koniger 2010) and the recognition that Raman spectroscopy is very sensitive to both H_2O and CO_2 under both subcritical and supercritical conditions (Cabaco 2007, 2010a, 2010b). Two specific goals of the Task were (1) to determine whether the technique can be used to substantiate thermal diffusion in CO_2-water mixtures and, if so, (2) to quantify the Soret effect as a function of conditions.

1.2 Summary of ZERT I results

In ZERT I, a specially designed high-pressure Raman cell suitable for supercritical studies with an imposed temperature gradient, specifically a 10-20^{o}C temperature gradient across an optical window through which Raman measurements could be acquired as a function of position, was built and applied to CO_2-water mixtures over a range of experimental conditions. Results were inconclusive over the range of conditions studied. In particular, even though variations in composition (CO_2 in H_2O) were measured between the two temperatures across the cell, the magnitude of the variations was very small. Soret coefficients calculated from this data were on the order of 10^{-3}, several orders of magnitude less than expected from published values of the ordinary and thermal diffusion coefficients of the components (Xu 2003; Amirkhanov 1987; Swinney 1968).

The surprisingly small values of S_T were attributed to two experimental difficulties. The first involved the design of the Raman cell, which appeared to offer insufficient thermal management under the imposed temperature gradient. The large size of the cell and its windows were speculated to induce convection currents that interfered with the measurements by evening out the concentrations across the cell. The second problem related to the range of compositions of the mixtures that were “accessible” in the study. The solubility of H_2O in scCO_2 is too low (mole fraction ~ 10^{-3}) to obtain Raman spectra with sufficient S/N for quantitative measurements. On the other hand, CO_2 dissolves in liquid H_2O to a degree that is an order of magnitude higher under similar pressure and temperature conditions. Research under ZERT II addressed these difficulties as follows: (1) a new Raman cell was designed and built with a smaller volume, better spatial resolution, and improved thermal management through the use of temperature-controlled windows, and (2) measurements were largely confined to the system “CO_2 dissolved in water” under conditions where CO_2 is either liquid or a supercritical fluid.

1.3 Justification and description of approach for ZERT II

The Raman cell in ZERT II consisted of a set of three concentric tubes. The CO_2-water mixture was contained in the annulus (white region in Figure 1) between a tube of transparent sapphire on the outside, which also served part of the optical window, and an inner tube of stainless steel on the other. Temperature-controlled water circulated through the outer annulus between the sapphire tube and an outer tube of transparent quartz (blue region in Figure 1) and also through the inner stainless steel tube (red region in Figure 1). With the two water streams held at two different temperatures by external temperature controllers, a temperature gradient was established across the inner annulus containing the

CO_2-water mixture. A simplified schematic of this Raman cell and the scattering configuration is shown in Figure 1.

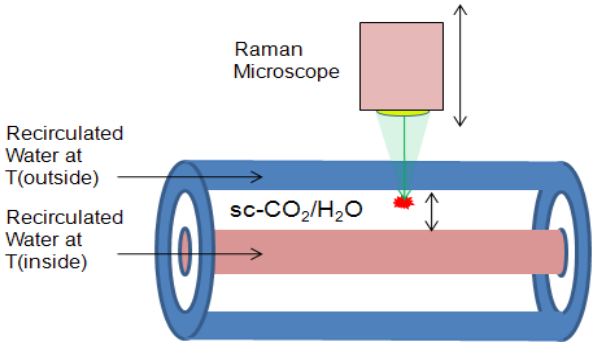

Figure 1. Simplified schematic of concentric-tube Raman cell.

A high-resolution UV-Raman microscope system was used to make the measurements in this study. The beam was focused within the bulk of a static CO_2-water solution contained in the inner annulus of the concentric-tube cell, positioned directly under the Raman microscope. As describe above, the central stainless steel tube and the outer annulus contained water at near-ambient pressure circulated between two thermostatically controlled temperature baths, separated in temperature by the desired gradient for the Soret study. The result was a temperature gradient imposed across the solution in the inner annulus ***without the presence of thermally unregulated windows***. Thermal regulation of the windows is one of the features that distinguished this design from that of the cell employed in ZERT I. The optical window consisted of the outer quartz tube, the circulating water circulating through the outer annulus, and the sapphire tube containing the CO_2-water solution.

Using the microscope, Raman spectra were collected as a function of depth, or distance between the thermally controlled walls of the inner annulus containing the CO_2-water solution. From these measurements, composition profiles (based on spectral features from CO_2 and water) within the solution and across the inner annulus were determined and, from the imposed temperature gradient, the occurrence and magnitude of the Soret effect was determined.

The depth resolution of Raman microscopes have improved significantly over the past few years, particularly with the advent of UV-Raman spectroscopy. PNNL recently acquired a Horiba Jobin Yvon LabRAM HR high-resolution UV-Raman system that was considered suitable for these measurements. This instrument, which has all reflective optics providing excellent quality Raman spectra with minimal signal distortion and resolution of +/- 2 cm^{-1}, also has distinct advantages in depth profiling. Studies on polished Si have demonstrated (Horiba Jobin Yvon Raman Application Note 2011) depth resolution of a fraction of a micrometer is achievable, depending on the excitation wavelength (shorter is better and our system uses deep-UV excitation at 244 nm), the characteristics of the material under study and the configuration of the optics, especially the size of the pinhole used for confocal measurements. In these measurements where a larger pinhole was required to achieve acceptable signal strength, we estimated a sampling volume (taken as spherical) with a diameter of about 500 μm. Although significantly poorer than anticipated, this depth-resolution was more than adequate to obtain several Raman spectra as a function of reasonable distinct distances between the two temperature reservoirs.

2.0 Experimental Procedure

2.1 Concentric-tube Raman cell design

The Raman cell used in these experiments was designed to withstand pressures of 10 MPa at temperatures up to about 45°C. This allowed measurements to be obtained on mixtures of CO_2 and water at 10 MPa (above the critical pressure of CO_2, 7.38 MPa) and temperatures in the regions below and above the critical temperature of CO_2 (31.04°C). The cell consisted of three concentric tubes: an outer tube made of quartz, a middle tube of sapphire and an inner tube of 316 stainless steel. A diagram of the configuration with dimensions of the components is given in Figure 2.

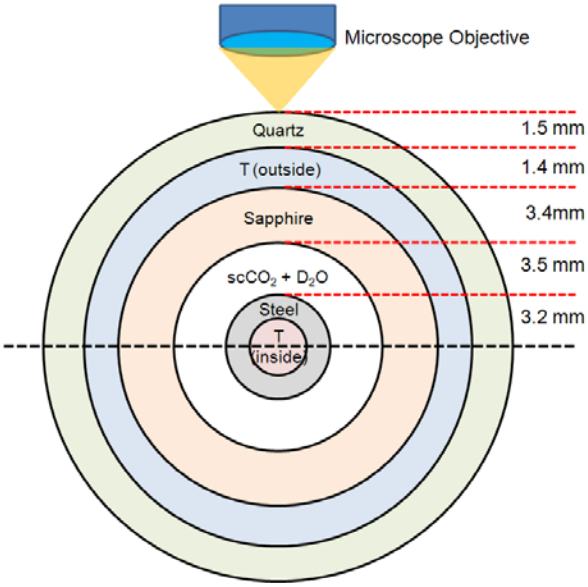

Figure 2. Concentric-tube Raman cell in cross-section showing thicknesses of the tubes and the annuli.

The steel tube in the center (gray in Figure 2) was used to carry constant temperature water (red in Figure 2), at T(inside), controlled by a Julabo (Vista, California) F12ED Refrigerated/Heating Circulator. The outer annulus with an outer wall of quartz (green in Figure 2) and an inner wall of sapphire (tan in Figure 2) contained water (blue in Figure 2) controlled at the second temperature T(outside) set with a separate Julabo circulator. The inner annulus contained the static mixture of CO_2 and water. It had an inner wall of steel (controlled at T(inside)) and an outer wall of sapphire (controlled at T(outside)). The dimensions of the sapphire tube were those required to withstand pressures up to 10 MPa and temperatures to 45°C. Pressure testing of the system was performed with water and nitrogen gas prior to the experiments to establish compatibility of this design with the test conditions.

In each measurement, the laser beam was imaged at different positions within the inner annulus containing the CO_2-water mixture. In this configuration, there were three components of the optical windows: (1) the outer quartz tube, (2) the thermally regulated H_2O circulating in the outer annulus, and (3) the sapphire tube. Since one of these components was H_2O, it was necessary to modify the procedure so that water in the inner annulus could be distinguished spectroscopically from water in the window. Consequently, D_2O was used in place of H_2O in most of the mixtures under study (i.e., in the inner

annulus). Figure 3 shows the spectra of H_2O and D_2O in the spectral region under study. Positions of the principal peaks of CO_2 (the Fermi dyad) are also shown to illustrate that all of the key peaks of these three Raman-active components (CO_2, D_2O, and H_2O) can be distinguished when all are present together. Sapphire also gave rise to distinct Raman bands that, with the one exception discussed below, are also sufficiently spaced from the peaks of the solution components to be unambiguous.

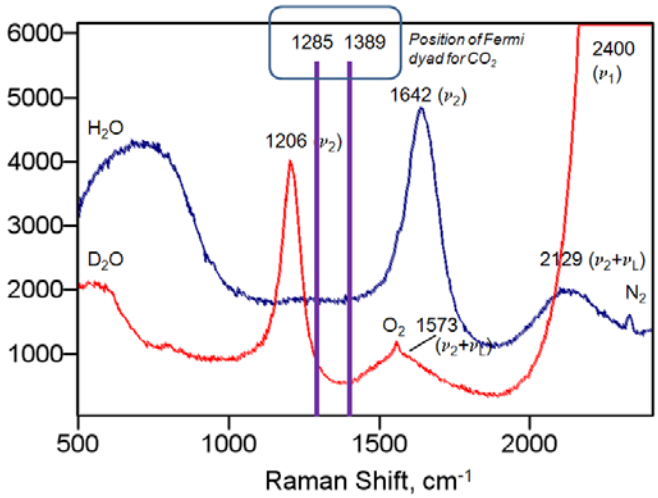

Figure 3. Comparisons of the UV-Raman spectra of H_2O and D_2O, at room temperature and atmospheric pressure, with the principal peaks of CO_2 (Fermi dyad) also shown.

The sapphire tube was purchased from Saint-Gobain (Hiram, Ohio) in a 6-inch length, machined slightly at the ends, and capped with specialized Swagelok (Solon, Ohio) 316 stainless steel fittings at the ends using Viton seals. The specialized fittings allowed a length of ¼ inch outside diameter. stainless steel tubing to be inserted through the center of the sapphire tube (used for carrying one of the circulated water streams) and also accommodated a section of stainless steel tubing at 90° to the sapphire tube (used for filling/emptying the cell with the CO_2-water solution). Approximately 1 inch at each end of the sapphire tube was retained within the fittings, leaving approximately 10 cm exposed for imaging and spectral study. A wider-diameter quartz tube was used as the container for the outer circulated water stream. It was equipped with quartz-tube side ports (for connecting to the circulator) and was sealed to the sapphire tube at the ends with epoxy. Remaining cell parts included 316 stainless steel fittings, valves and tubing purchased from Swagelok Inc. as well as a Cecomp Electronics (Libertyville, Illinois) digital pressure gauge, assembled as shown in Figure 4. An ISCO Inc. (Lincoln, Nebraska) 1000D pump was used to pressurize the cell with the CO_2-water mixtures. The cell assembly was mounted on a floating optical table using position-adjustable Newport Inc. (Irvine, California) stages to provide stability and facilitate alignment of the laser beam on the sample. Lexan blast shields were incorporated for safety. A photograph of the assembled cell (positioned under the UV-Raman microscope) is shown in Figure 5. The volume of the cell and all tubing leading from (but not including) the pump and to a Tescom (Elk River, Minnesota) back pressure regulator, used to control back pressure and empty the cell, was approximately 70 mL. The D_2O used in the study was 99.9% pure and obtained from Sigma-Chemical Company (St. Louis, Missouri), while the CO_2 gas was 99.99% pure and purchased from Polar Cryogenics (Portland, Oregon).

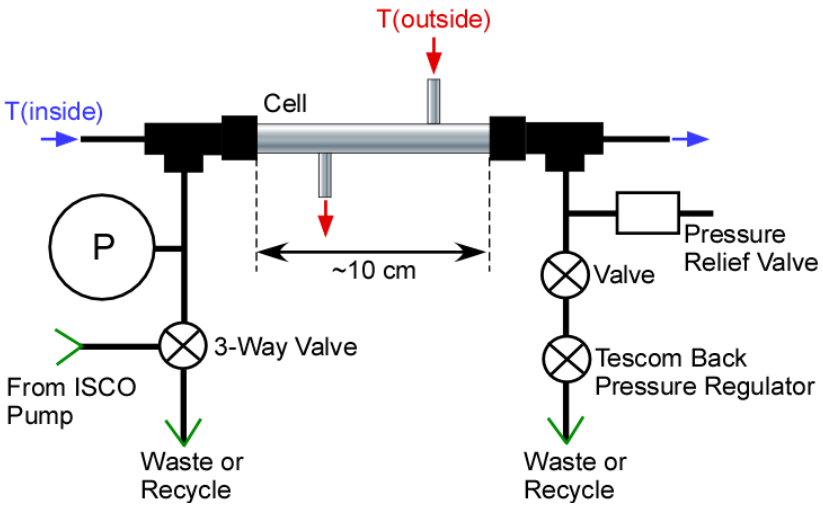

Figure 4. Schematic of the concentric-tube Raman cell within its assembly.

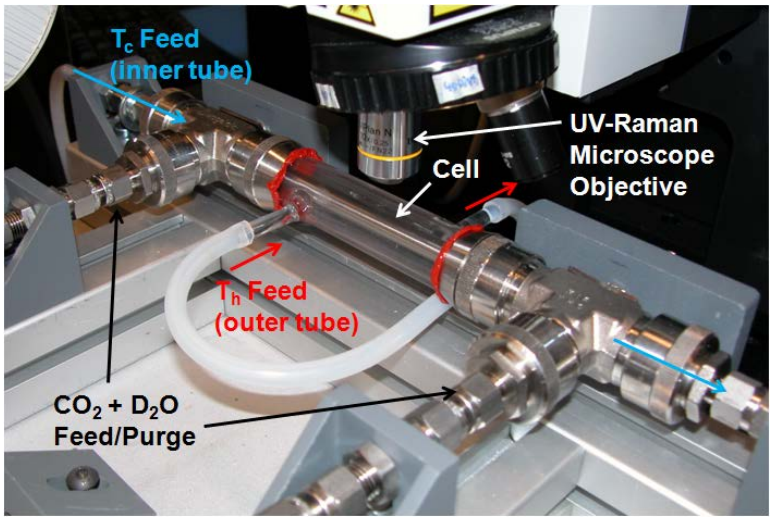

Figure 5. Photograph of the concentric-tube Raman cell assembly positioned under the UV-Raman spectrometer microscope objective.

To minimize specular reflection and elastic scattering from the stainless steel tube (both are potential interferences in Raman spectroscopy), the stainless steel tube was coated with black oxide using a proprietary method similar to "bluing." The resulting coating, consisting of transition metal oxides, was black and gave no significant Raman spectrum in the region of interest. Figure 6 illustrates the degree to which specular reflection was attenuated by the coating.

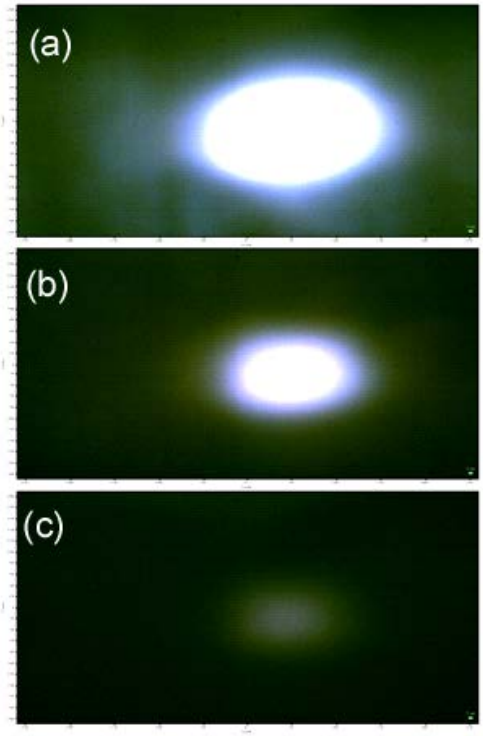

Figure 6. Images of the reflected laser light from the stainless steel tube in the center of the Raman cell, (a) with the incident light focus on the bare steel, (b) with the incident light focused on the steel with a high-temperature air-formed film (held at 600°C overnight), and (c) with the incident light focused on a "blued" steel surface.

2.2 UV-Raman spectrometer

Raman spectra were collected using a Horiba JY (Edison, New Jersey) LabRAM HR (high-resolution) Raman (confocal) microscope system. With a focal length of 0.8 m and dual gratings with groove density of 2400 grooves/mm the instrument can achieve a nominal spectral resolution of 1-2 cm^{-1}. Excitation was provided by the deep-UV 244-nm line of a Lexel (Fremont, California) Model 85-SHG frequency-doubled Ar^{+} ion laser equipped with a non-linear beta barium borate (BBO) crystal. Laser power was 25 mW at the source and approximately 1 mW at the objective. Significant further attenuation of power is expected through the Raman cell. A 10x UV-compatible microscope objective (numerical aperture = 0.25) with a working distance of 15 mm was used. The spectrometer pinhole was kept fairly large, at 400 μm, resulting in less-than-optimal depth and lateral resolution. However, laser throughput was improved with the larger pinhole, giving acceptable band intensities when collected with an exposure time of 500 s. The spectral range was restricted to Raman shift above 450 cm^{-1}. Measurements at lower frequencies were not possible because of the presence of a factory-installed edge filter for eliminating the exciting line. Spectral analysis, including curve fitting, was performed using Thermo Scientific (Waltham, Massachusetts) Grams/32 AI software. Any curve fitting used the Levenburg-Marquardt non-linear peak fitting method (Levenberg 1944) with baseline correction to remove background from Rayleigh scattering or fluorescence. A photograph of the spectrometer with a cell positioned for data collection is given in Figure 7.

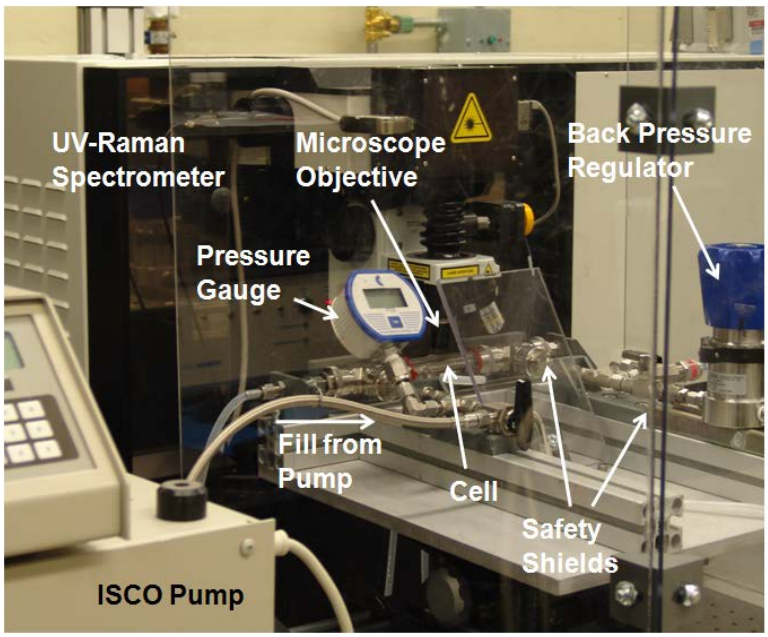

Figure 7. Photograph of the concentric-tube Raman cell assembly, UV-Raman spectrometer, and ancillary equipment.

2.3 Typical experiment and variables

The following procedures were used in the collection of spectra in most of the experiments:

- The pump, then cell, were filled with pure D_2O under ambient conditions and pressurized to the pressure of the experiment, 10 MPa. The cell was then valved off from the ISCO pump.
- The pump pressure was reduced to the pressure of the CO_2 cylinder and the volume of D_2O remaining in the pump was noted. A volume of CO_2 gas at this pressure (approximately 5.8 MPa) was then added to the pump to give the required concentration of CO_2 in the final test mixture. Following this, the pump was sealed off from the CO_2 cylinder and the pump pressure increased to 10 MPa. To help mix the CO_2 and D_2O, the pressure in the pump was dropped back to 5.8 MPa and then returned to 10 MPa, and this procedure was repeated approximately five times.
- The mixture in the pump was allowed to sit overnight so the CO_2 could dissolve in the D_2O at 10 MPa. During this time, the cell itself still contained pure D_2O at 10 MPa.
- On the following day, the valve between the pump and cell was opened, and the mixture in the pump was slowly metered into the cell to replace the pure D_2O in the cell. The metering was done by slowly opening and closing the pressure reducing valve at the exit of the cell. The procedure was performed carefully to minimize any flashing of CO_2 in the cell. Done properly, the solution in the cell remained homogeneous with no gas bubbles or liquid CO_2 separating from solution. (Phase separation was evident by the appearance of a second phase in the sapphire tube.) After flowing about 150 mL through the cell, the cell was considered completely charged with the fluid mixture. The pump remained on and connected to the cell to maintain pressure at 10 MPa throughout the experiment.
- The temperature controllers were turned on and thermostated water was circulated through the two thermal reservoirs at the desired temperatures.

- Raman spectra were collected after waiting at least two hours for thermal equilibration.
- The Raman spectrometer was first calibrated by focusing on the sapphire tube and using the Raman bands of sapphire (e.g., the strong sapphire peak at 746 cm^{-1}).
- The microscope objective was then moved so that the bottom of the sapphire tube was put in visible focus using an objective suited to visible light. This position was defined as z = 0 μm.
- The UV objective was then substituted, with its position configured to retain z = 0 μm, at the focal position without further adjustment of the microscope.
- Raman spectra were acquired as a function of position across the annulus containing the CO_2-D_2O solution. The first measurement was usually obtained at the inside surface of the sapphire tube (z = 0), taken as T = T(outside), or very near to it (z = 200 μm). Subsequent measurements were usually made at increments of 200 μm from this position (here reported as positive values of z) and toward the stainless steel tube (shown to be at z = 2000 μm, as discussed below), where T = T(inside). Because of optical and cell geometry constrains, no independent temperature measurements could be made at the exact positions from where the spectra were acquired. However, calculations predicted that minimal temperature drop occurred across the sapphire and the stainless steel tubes, so the assumption of thermal equilibration between the temperature reservoirs and fluid at z = 0 and z = 2000 μm was considered valid.
- Immediately after collecting Raman spectra in the increasing-z direction, a series of spectra were collected in the decreasing-z direction ending up at the position z = 0, or close to it.

Some experiments employed special procedures as follows:

- To lower the possibility of condensation of water vapor on the outside of the cell, T(outside) was usually kept higher than T(inside). Some experiments used T(inside) greater than T(outside) to make sure that there was no unexpected effect of the direction of the thermal gradient.
- A series of experiments were performed with T(outside) = T(inside) to account for the possibility of any spectral variations across the annulus in the absence of an applied temperature gradient.
- A series of experiments were performed with the outer quartz jacket removed. This permitted the use of CO_2-H_2O instead of CO_2-D_2O mixtures since there was no spectral interference from the H_2O in the outer thermal reservoir. The configuration had the added advantage of much higher signal-to-noise since there was no loss of signal by scattering from the quartz, reservoir water, and the accompanying interfaces. In these experiments, T(outside) was taken at the value measured on the outside of the sapphire tube with a thermocouple.
- A series of experiments (2-position measurements) were performed on a given CO_2-D_2O mixture in which spectra were acquired at two positions (e.g., z = 500 μm and 2000 μm) with varying temperature gradients imposed across the cell. T(inside) was held constant while T(outside) was changed). These experiments provided data on a single mixture over a wider variety of thermal conditions than those in which more extensive data as a function of z were acquired.
- Mixtures of D_2O dissolved in $scCO_2$, instead of CO_2 dissolved in D_2O or H_2O, were also performed. These were considered more challenging for two reasons: (1) the solubility of D_2O in $scCO_2$ was about an order of magnitude less than CO_2 in D_2O (mole fraction 10^{-3} vs. 10^{-2}) under the same conditions of temperature and pressure (i.e., 10 MPa, and 12°C to 45°C), (2) with mostly $scCO_2$, the

amount of stored energy in the cell increased significantly and, with it, the level of safety concerns. Nevertheless, experiments of this sort were still conducted to determine if D_2O could be detected at these concentrations (the stronger C-D stretching bands were used in an attempt to compensate for the lower concentration) and, if so, whether a Soret effect was observed at "the other end" of the phase diagram of the mixture.

- Some experiments used deuterated brine (D_2O + 1 M NaCl) instead of pure D_2O.

The key variables in this study were:

- ***Position*** (z) relative to the top of the sapphire tube. Values of z with increments of 200 μm were usually used.
- ***Direction of scan***, i.e., either increasing z or decreasing z. In most cases, data were collected in both directions during the same experiment.
- ***Values of temperature*** and ***size of temperature gradient***. In most cases, a given experiment spanned a temperature range below the critical point of CO_2 (31.04^{o}C) or above it, to avoid the effects of density fluctuations (on the relative intensities of the Fermi dyad components in CO_2) known to occur at this temperature. A series of two-position experiments were also conducted where the temperature gradient was changed in increasing increments, while making measurements at only two positions in the cell.
- ***Direction of temperature gradient***, i.e., T(outside) > T(inside) or T(inside) > T(outside).
- ***Concentration of CO_2*** in the mixture (i.e., mole fraction CO_2 or X(CO_2)). In most cases the concentration was kept below the solubility of CO_2 in H_2O (approximately 0.028 mole fraction under these conditions). Some experiments were run with H_2O saturated with CO_2. A few experiments were also performed with scCO_2 saturated with D_2O (i.e., X(H_2O) ~ 0.003). A solution of CO_2 dissolved ***in brine***, D_2O + 1 M NaCl, was also tested.
- A few experiments were conducted where ***pressure was varied*** while holding the temperature values constant.

3.0 Results

3.1 Assessment of Raman cell

3.1.1 Position of the microscope objective vs. focal point of the measurement

During preliminary testing, it became clear that increments in the vertical position of the microscope objective (denoted by the z value) did not correspond to increments in the position of the focus spot within the annulus of the cell. This is attributed to refraction of the laser beam through the three components of the window (quartz tube, water layer, and sapphire tube) between the objective and the fluid. It was estimated by Snell's law that the major deviation was caused by refraction through the relatively thick sapphire tube. Calculations indicated that a z value of 3000 μm actually corresponded to a distance of 2000 μm within the fluid, and this was born out by experiment. First, when using white light illumination, visual images of a "surface" were obtained at approximately these two locations (i.e., z = 0 and 2000 μm). Second, as shown in Figure 8 (for an experiment with $X(CO_2)$ = 0.0027, P = 10 MPa, and T(outside) = T(inside) = 40°C), the total integrated intensity of peaks (from both CO_2 and D_2O) at z = 0 μm is roughly half its maximum value and the sapphire peaks show a markedly sudden decrease in intensity. For z > 2000 μm, the total signal drops significantly due to focusing beyond the stainless steel tube, but does not completely disappear because there is still some out-of-focus Raman scattering.

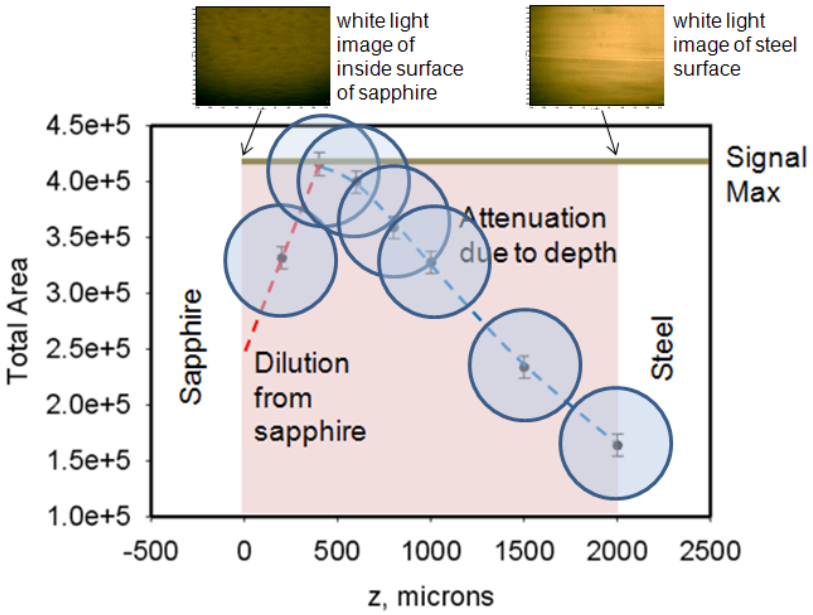

Figure 8. Total Raman scattering signal strength (from both CO_2 and D_2O) as a function of the position of the objective (z value). In relationship to position within the annulus, z = 0 μm corresponds to the inside surface of the sapphire tube, whereas z = 2000 μm is near the outside surface of the stainless steel tube. The photographs are white-light images at these two positions. Circles around each point indicate the approximate sampling volumes.

In each experiment, Raman spectra were acquired between z = 0 and z = 2000 μm (pink region in Figure 8), usually at increments of z = 200 μm. Given that width of the annulus was 3.4 mm, that the

range of z-values relevant to the annulus was 2000 μm, and also that the relationship between the two scales is probably non-linear, it was difficult to correlate exactly the position of the focused beam with the z value. However, the important variable in this study was temperature and not position. For this reason, we took the following approach in our analysis: (1) the spectrum corresponding to T(outside) was taken as the spectrum at z = 0 μm; (2) the spectrum corresponding to T(inside) was taken as the spectrum at z = 2000 μm; and (3) the spectra for positions with z between 0 and 2000 μm (pink region in Figure 8) were deemed to vary continuously between these two limits. To estimate the Soret coefficient, we used the spectra at the end points. If spectra at these positions could not be obtained directly, they were determined by extrapolation from the observed variations in the spectra within the annulus.

3.1.2 Estimate of sampling volume

Figure 8 also illustrates the effects of the two principal causes of signal attenuation in the Raman cell. The first was important for z values between 0 and 500 μm, where the Raman scattered signal was "diluted" by the contribution of the sapphire tube. Peaks from the sapphire (including the very strong one at 746 cm^{-1}) were still strong in this region due to contribution from significant out-of-focus scattering. At positions greater than 500 μm, almost all of the signal came from the fluid. The results not only explain the loss of signal near the sapphire tube, but help establish an approximate volume from which most of the scattering occurred. In the present case, the volume (approximated by a sphere) had a likely diameter of about 500 μm (or about 25% of the annulus distance). This suggests that increments less than z = 500 μm exhibit marked overlap of scattered signals. Since the total thickness of the annulus is 2000 μm, about 4 unique measurements were therefore possible across it, sufficient for a reasonably good estimate of a significant gradient in any of the spectral parameters. To illustrate this, a circle with a diameter of 500 μm is drawn around each data point in Figure 8. Even though the circles overlap, there is "enough z" represented to capture the variation across the annulus. The same could be argued for individual spectra collected at these positions.

For z values greater than about 500 μm but less than 2000 μm, the total signal strength again decreases. This is attributed to additional scattering of the Raman light as it *returns* to the objective from positions deep within the sample. The deeper the focal point, the more significant the losses will be from this phenomenon.

Finally, it is important to note that any changes in the *ratios of individual band intensities* (e.g., CO_2 band relative to D_2O band) arising from variation in composition of the mixture across the annulus should be unaffected by variations in the total Raman scattering signal. Consequently, the only effect that variations in the *total spectral intensity* will have on determining Soret coefficient is with regard to signal-to-noise. A smaller total scattering intensity, in most cases, resulted in a smaller signal-to-noise and a greater uncertainty in measured or calculated spectral parameters.

3.2 Raman spectra

3.2.1 Experiments on D_2O containing CO_2 below saturation

Raman spectra were obtained as a function of distance (related to the z value) across annulus containing the CO_2 + D_2O mixture with concentrations of CO_2 in D_2O below its solubility value. For the

conditions of this study, this value corresponds to $X(CO_2)$, approximately 0.028. The specific compositions studied in this work were $X(CO_2)$ equal to 0.0014, 0.0027, and 0.0054, corresponding to approximately 5%, 11%, and 22% of saturation. Spectra are shown in Figures 9 and 10 as a function of the z value $X(CO_2)$ = 0.0054, and 0.0027, respectively, and with two different temperature gradients. The results for 0.0014 showed similar trends but the CO_2 peaks were extremely weak. Spectra were also collected with different temperatures and temperature gradients applied. Generally, for a given experiment, the temperature gradient was maintained on one or the other side of the critical temperature, 31.1°C. For measurements below the critical point, the reservoir temperatures were 30°C and 12°C (clathrates form below 12°C); for measurements above the critical point, the temperature reservoirs were at 33°C and 45°C (the approximate upper limit for the cell). Spectra shown in Figures 9 and 10 are for one of the temperature gradients for each composition. Results for other temperature gradients showed the same results. Spectra collected upon increasing the z value are shown, although spectra for decreasing z, with all other conditions the same, were essentially identical.

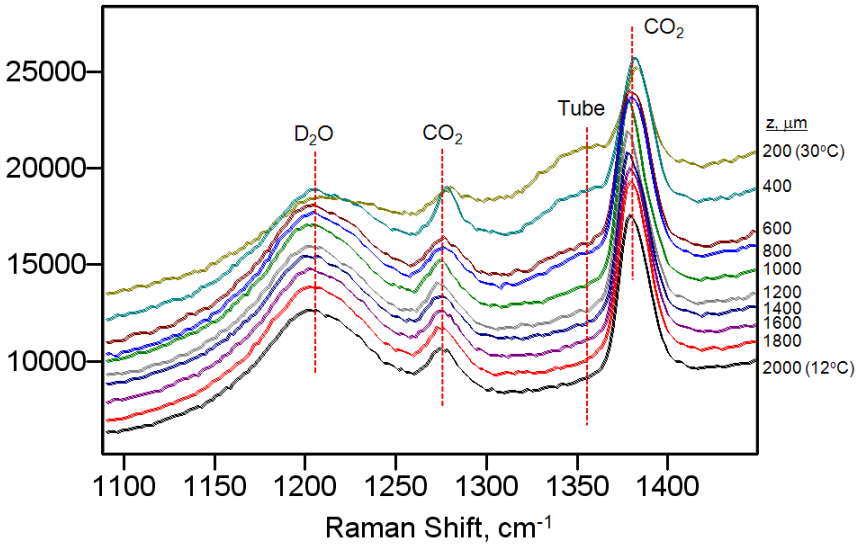

Figure 9. UV-Raman spectra as a function of position within the annulus (in terms of the microscope position, z), with $X(CO_2)$ = 0.0054, T(inside) = 12°C and T(outside) = 30°C. Higher temperature is outside. The spectra were acquired in the direction of increasing z. CO_2 is a liquid under these conditions.

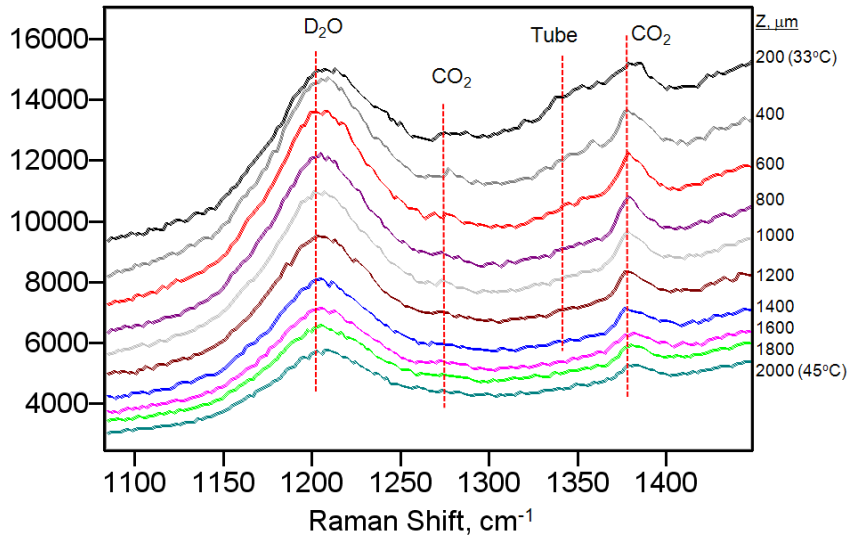

Figure 10. UV-Raman spectra as a function of position within the annulus (in terms of the microscope position, z), with X(CO_2) = 0.0027, T(inside) = 45°C and T(outside) = 33°C. The higher temperature is inside. The spectra were acquired in the direction of increasing z. CO_2 is supercritical under these conditions.

Each spectrum in Figures 9 and 10 contains three bands of interest: the two peaks corresponding to the Fermi dyad of CO_2, positioned at approximately 1273 and 1377 cm^{-1}, respectively, and the band at 1203 cm^{-1} from the bending mode of D_2O. The band positions are a little lower than those indicated in Figure 3 for neat compounds, especially the Fermi dyad of CO_2. The variance, which was reproducible for all mixtures with concentrations of CO_2 below saturation, was surprising and its cause unknown at this time. However, as discussed later in this report, the peak frequencies from mixtures with high scCO_2 concentrations are closer to the values in Figure 3, suggesting the likely explanation involves molecular interactions, arguably different for CO_2 surrounded by other CO_2 molecules (at high CO_2 concentration) and CO_2 surrounded by water molecules (at low CO_2 concentration).

A band at approximately 1350 cm^{-1} also appears in the spectra for measurements taken close to the sapphire tube (small z). The Raman spectrum of sapphire does not normally have a peak at this frequency, however no published spectra of sapphire with UV excitation have been previously reported, to our knowledge. It is possible that the peak is due to sapphire, observed here because of resonant enhancement in the UV. Another possibility is that it arises from a carbon impurity associated with the surface of the sapphire. Amorphous carbon has a strong peak due to sp^3 carbon (C-C stretch) at approximately 1360 cm^{-1}. Regardless of the cause, this peak appears to be associated with the surface of the sapphire and is disregarded in this study. Another observation that may be of fundamental significance, but is not addressed further in this study, is the apparent asymmetry of some of the peaks, particularly the stronger Fermi dyad component at 1377 cm^{-1}, in spectra of mixtures where the CO_2 peaks are weak relative to D_2O (see Figure 10). This characteristic of the Fermi dyad probably relates to molecular interactions and how they change with concentration, particularly when CO_2 concentrations are low. Similar to the effect on peak frequencies, reported above, a definitive explanation of the band shape is not forthcoming from this study, nor is it within its scope.

The primary objective of this study was to determine whether changes in the Raman spectra occur as a function of position across the annulus when a temperature gradient is applied. ***As indicated by Figures 9 and 10, the spectra exhibit no obvious changes as a function of position (other than overall intensity changes and changes related to the contribution from extraneous bands) for a given solution composition. This is the first qualitative evidence that a Soret effect is not inordinately pronounced for solutions studied in this work.***

Several characteristics of the spectra, including relative peak areas, intensities and band shapes, were scrutinized quantitatively and none showed significant change across the annulus. Figure 11, for example, shows the variation of the ratio of the intensity of the strongest peak in the Fermi dyad of CO_2 (1377 cm^{-1}) to the intensity of the peak due to D_2O (1203 cm^{-1}) for solutions with $X(CO_2)$ = 0.0014 and 0.0027. Figure 12 shows the variation in the same ratio for solutions with $X(CO_2)$ = 0.0054. Data for several temperature gradients are shown, as are data from experiments with increasing-z and decreasing-z, and with the gradient imposed in two directions (higher temperature inside and outside). The results all point to the same conclusion: regardless of the way the experiment was performed, there was no significant variation of the intensity ratio across the annulus for a given value of $X(CO_2)$. (Variation of the ratio with the $X(CO_2)$ value of each experiment is discussed later in this report.) Uncertainties were taken as twice the standard deviation of the intensity of peaks calculated from the curve fits. Note that the uncertainties are much greater for small z. This is due to the relative weakness of the bands in spectra acquired at these locations, as well as the need to subtract a correspondingly larger background with stronger extraneous bands (i.e., from the sapphire tube) in determining the CO_2 and D_2O peak intensities.

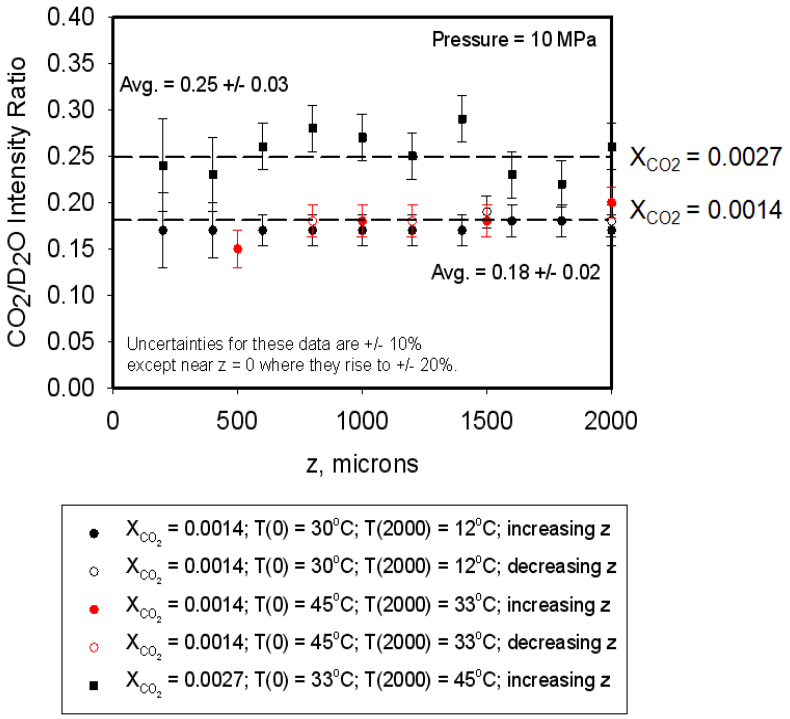

Figure 11. CO_2/D_2O peak intensity ratio calculated from the Raman spectra as a function of position for $X(CO_2)$ = 0.0014 and 0.0027, with different temperature gradients and direction of scan.

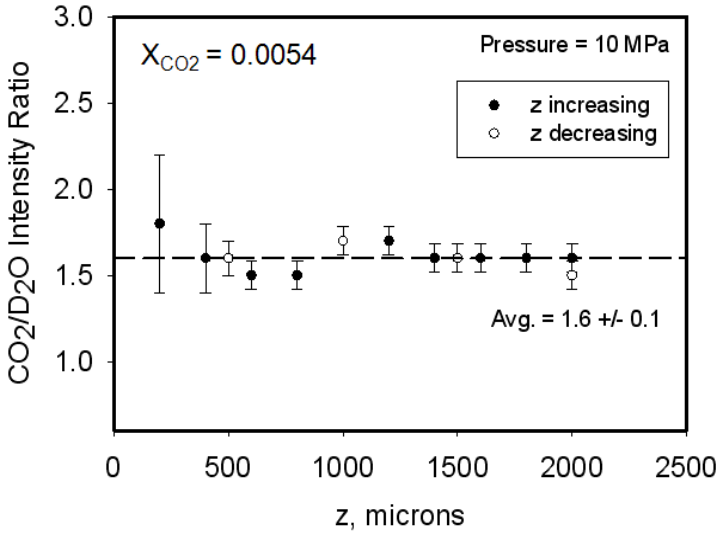

Figure 12. CO_2/D_2O peak intensity ratio calculated from the Raman spectra as a function of position for $X(CO_2)$ = 0.0054, T(outside) = 30°C and T(inside) = 12°C, in both increasing- and decreasing-z directions.

Spectra as a function of z were also acquired in a series of experiments where the same temperature was imposed on both sides of the annulus, i.e., T(outside) = T(inside). Results from two of these studies, at 23°C and 40°C, are shown in Figure 13. The intended purpose of these "isothermal" measurements was to address questions that might arise in the event the relative Raman intensities showed a significant and reproducible trend as a function of position within the annulus. In particular, could this variation be due to something other than the temperature gradient? Given the lack of variation shown in Figures 11 and 12, the results in Figure 13 are expected, and therefore, somewhat academic. They also show no significant difference in the Raman intensity ratio as a function of position across the annulus.

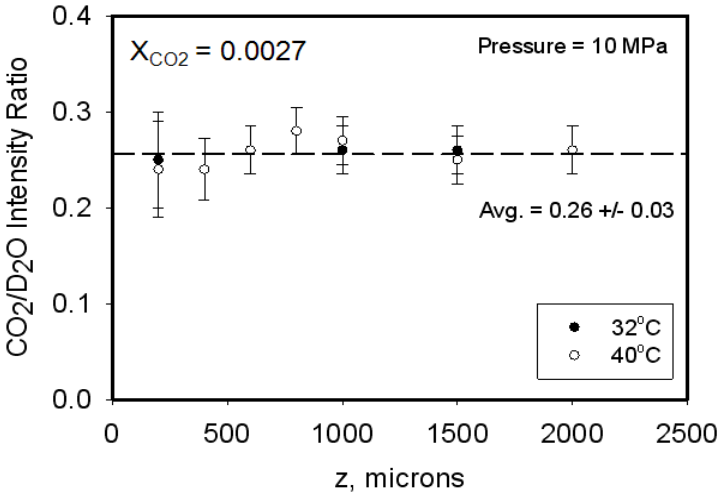

Figure 13. CO_2/D_2O peak intensity ratio calculated from the Raman spectra as a function of position for $X(CO_2)$ = 0.0027 with T(outside) = T(inside) at 32°C and 40°C. Spectra were collected in the direction of increasing z.

As a further confirmation of the lack of significant variation in the relative Raman intensities across the annulus, a series of "2-point temperature ramps" were performed. In this study, Raman spectra of a CO_2-D_2O mixture were obtained at only two positions (z values) within the annulus containing a given solution but using different temperature gradients. For the data in Figure 14, T(outside) was held at 45°C and T(inside) was varied as indicated. A Raman spectrum was acquired at the two positions for each gradient, after allowing sufficient time (about 2 hours) for thermal equilibration. The spectra shown in the figure were background-adjusted and intensity-normalized so the D_2O peak overlapped for measurements at the two positions (different color correspond to the different temperature gradients and positions). Inspection of the CO_2 peaks under these conditions indicates no significant change in the spectra results from changing the temperature gradient over a significant range of values, other than the single case (red spectrum in Figure 14) that appears to have a slightly smaller background toward higher frequencies. The results are consistent with the spectra in Figures 9-13 that showed no significant variation in the relative intensities of the CO_2 and D_2O peaks across the annulus.

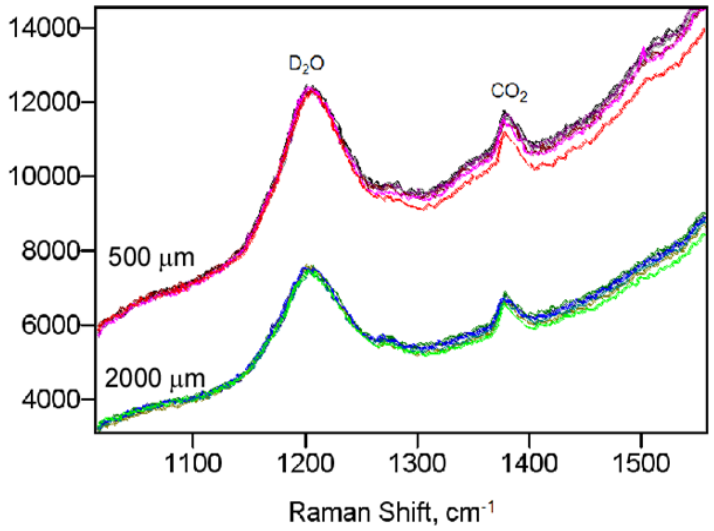

Figure 14. UV-Raman spectra at two positions within the annulus with X(CO_2) = 0.0027 and T(outside) = T(0 μm) = 45°C and with varying T(inside). Spectra are shown for T(inside) = T(2000 μm) = 45°C, 40°C, 35°C, 30°C, 25°C, and 20°C.

3.2.2 Experiments on D_2O + 1 M NaCl containing CO_2 below saturation

Results similar to the aforementioned experiments, but using 1 M NaCl in D_2O instead of pure D_2O, are shown in Figure 15. The presence of the NaCl does not appear to make a difference in the response of the Raman intensity ratios to a temperature gradient imposed across the annulus. Similar to results without the NaCl, there is no significant change in the intensity ratios.

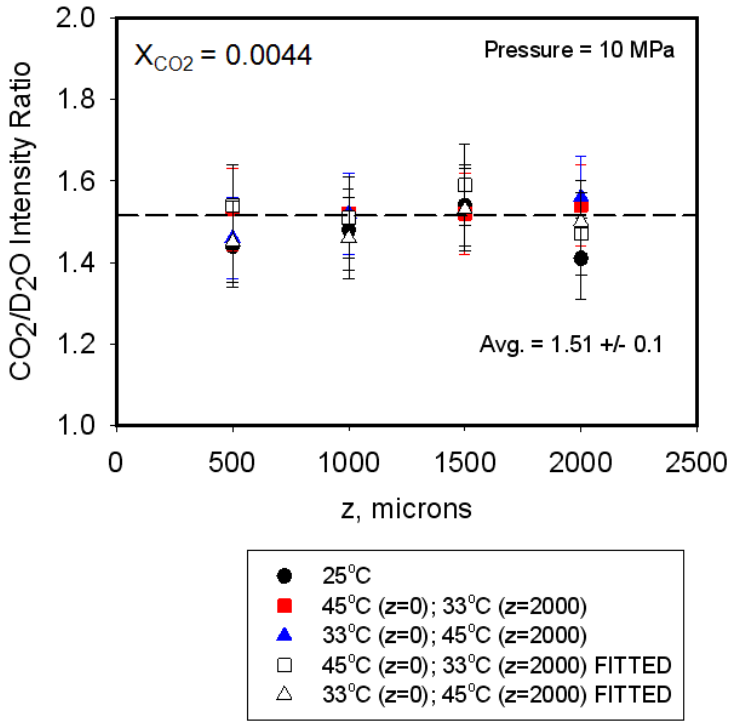

Figure 15. CO_2/D_2O peak intensity ratio, for solutions containing 1 M NaCl, as a function of position with $X(CO_2)$ = 0.0044, and various temperature gradients. Open symbols are ratios for the same experiments as the corresponding closed symbols, but were calculated using integrated intensities from curve fitting results.

3.2.3 Varied pressure study

Raman spectra were also acquired in an experiment with $X(CO_2)$ = 0.0027 and temperature held constant at 40°C (above the critical temperature with no temperature gradient), but where the cell pressure was changed. The purpose of this experiment was to see if pressure had an effect, independent of concentration, on the relative intensities of the CO_2 and D_2O bands. The lowest pressure studied was 1 MPa, where the solubility of CO_2 in water at 40°C is approximately 0.004. Since $X(CO_2)$ = 0.0027, a single phase was maintained throughout this study and this was confirmed by the absence phase separation in the cell at any time. Spectra were measured in the center of the cell (z = 1000 μm) for each pressure. The results, shown in Figure 16, indicate that there was no significant variation in the CO_2/D_2O intensity ratio with cell pressure, for a single-phase solution, over the range of pressures studied in this work.

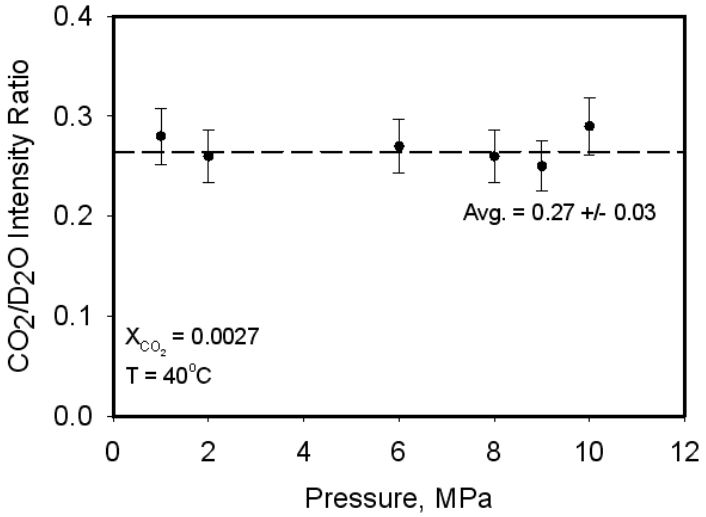

Figure 16. CO_2/D_2O peak intensity ratio, for solution with $X(CO_2) = 0.0027$ and T(inside) = T(outside) = 40°C, as a function of cell pressure.

3.2.4 H_2O containing CO_2 at saturation

Raman spectra as a function of position across the annulus, between T(inside) = 11°C and T(outside) = 15°C, were also obtained for a solution of H_2O saturated with CO_2 at 10 MPa and the two temperatures, roughly corresponding to $X(CO_2) = 0.029$ and 0.028, respectively. The results are shown in Figures 17 and 18.

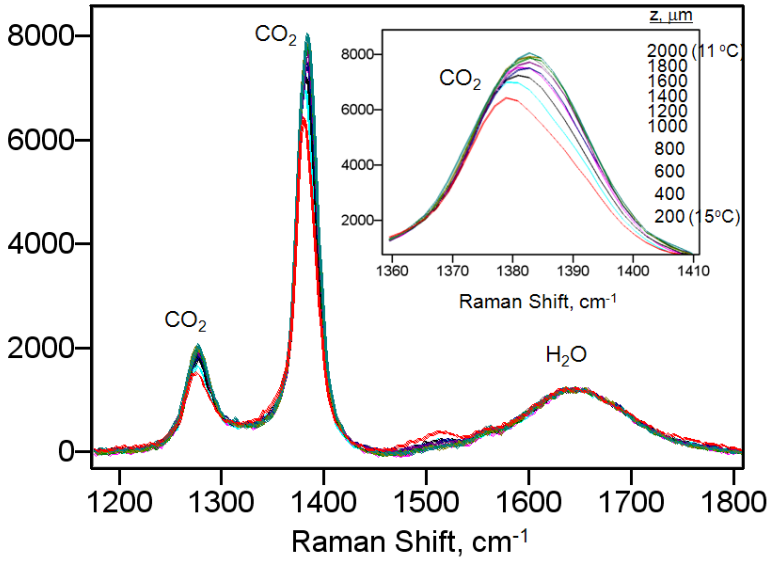

Figure 17. UV-Raman spectra as a function of position within the annulus (in terms of the microscope position, z), for H_2O saturated with CO_2, i.e., $X(CO_2) \sim 0.028$. T(inside) = 11°C and T(outside) = 15°C. Spectra were acquired in the direction of increasing z. Spectral intensities are normalized with respect to the H_2O peak at 1640 cm-1.

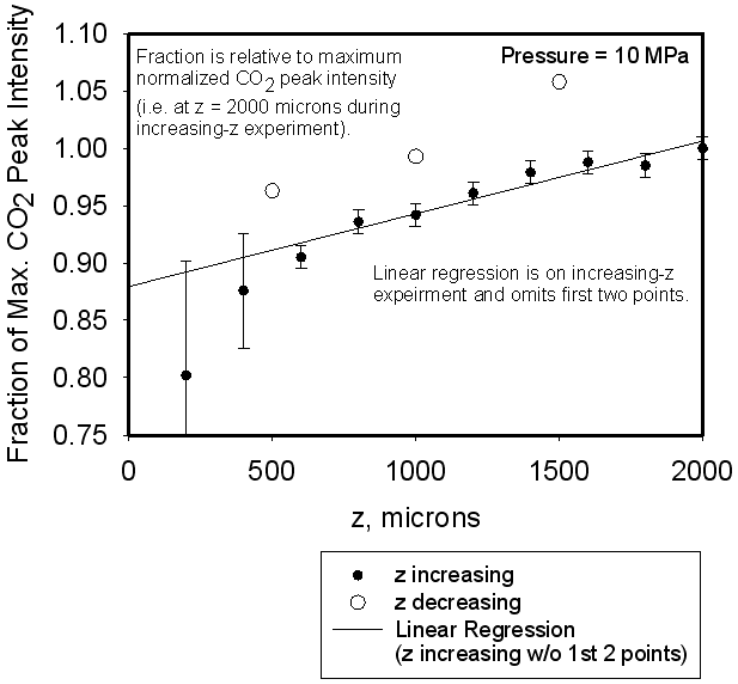

Figure 18. $CO_2/(CO_2 + D_2O)$ peak intensity fraction calculated from the Raman spectra as a function of position, for H_2O saturated with CO_2, i.e., $X(CO_2) \sim 0.028$. Results are shown for measurements made with both increasing and decreasing z. Linear regression in the absence of the two low-z points is shown.

H_2O was used instead of D_2O in these studies because they were performed in the absence of the outer temperature reservoir. T(outside) was controlled by the air temperature and measured with a thermocouple as equal to 15°C. Unlike the experiments on solutions with lower concentrations of CO_2, these results show a clear trend with changing z. The ratio of intensities of the CO_2 to H_2O peaks increases in going from the higher temperature side, T(outside) or z = 0 μm, to the lower temperature side, T(inside) = 11°C or z = 2000 μm. Because the CO_2 peaks are so large in this study, it was more prudent to plot the CO_2 peak intensity (1389 cm^{-1}) in terms of the fraction of total intensity of the H_2O (1640 cm^{-1}) + CO_2 (1389 cm^{-1}) peaks, rather than using the CO_2/H_2O intensity ratio. The results, shown in Figure 18, clearly illustrate the significant and consistent trend in the relative size of the CO_2 peak as function of position, and therefore temperature, within the annulus. Assuming the relative intensity scales with concentration, Figure 18 indicates a preferential segregation of CO_2 to the colder side of the annulus in this experiment.

3.2.5 $scCO_2$ containing D_2O at saturation

Experiments were also performed on the other side of the phase diagram of the CO_2-water solution, i.e., with D_2O dissolved in $scCO_2$. The CO_2 was the majority species in these studies and was in the supercritical state. Since the solubility of D_2O in $scCO_2$ is much lower than CO_2 in D_2O, i.e., $X(D_2O) = 0.003$ compared to $X(CO_2) = 0.028$ to 0.029, under similar conditions, using the C-D stretching mode, instead of the much weaker bending mode, for quantitative analysis seemed prudent. The results of a series of measurement across the annulus of one of these studies, with T(outside) = 40°C and T(inside) = 32°C, are shown in Figure 19.

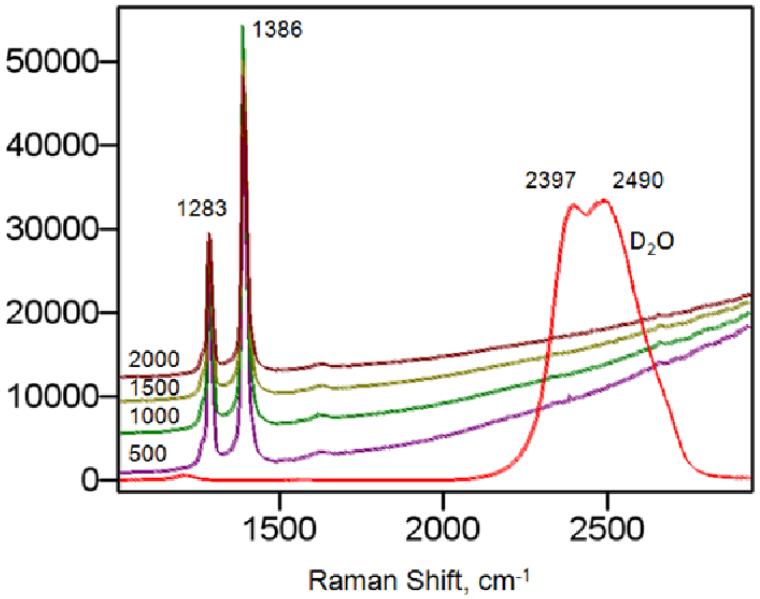

Figure 19. UV-Raman spectra as a function of position within the annulus for solutions of $scCO_2$ containing D_2O at saturation (i.e., $X(D_2O) \sim 0.003$). T(inside) = 32°C and T(outside) = 40°C.

As expected from the concentration, the CO_2 Fermi dyad is very strong in these spectra. Unfortunately, the D_2O peaks are also extremely weak. The expected position of the C-D stretching bands, around 2500 cm^{-1}, is illustrated by the spectrum of neat D_2O that is also plotted in the figure. It is difficult to discern even the slightest contribution from these modes to the spectra obtained from the solution, precluding the determination of the relative intensities of bands from the two components and, consequently, concentration trends across the annulus.

4.0 Discussion

4.1 Solutions of CO_2 in D_2O with CO_2 below saturation

Raman spectra showed no significant variation with respect to the relative intensities and areas of peaks associated with CO_2 and D_2O as a function of position within the cell annulus between the two imposed temperatures, regardless of the concentration of CO_2, as long as it was below saturation. The behavior was obtained independent of the direction of the scan (increasing or decreasing z), the size of the temperature gradient (between 11°C and 45°C), whether the data was collected below or above the critical temperature of CO_2, the direction of the temperature gradient (higher temperature or colder temperature on the outside), pressure (up to 10 MPa), or in the presence of 1 M NaCl. These results argue to the presence of no detectable Soret effect, corresponding to $S_T \sim 0$ within the uncertainty of the measurements.

An estimate of uncertainty in S_T can be obtained by inspection of the uncertainties in the intensity ratio vs. z-position plots. As illustrated in the case of the study with X(CO_2 = 0.0014), T(outside, z = 0 μm) = 30°C and T(inside, z = 2000 μm) = 12°C, shown in Figure 20, straight lines are easily drawn to bracket the error bars in an experiment. We now make use of Equation (3), after rearranging and integrating between the two temperatures T_o = T(outside, z = 0 μm) = 30°C and T = T(inside, z = 2000 μm) = 12°C where concentrations are c_o and c, respectively:

$$\ln\left(\frac{c}{c_o}\right) = -S_T\left(T - T_o\right) \tag{4}$$

or, in terms of the absolute magnitude of S_T:

$$\left|S_T\right| = \left|\left[\frac{1}{\left(T - T_o\right)}\right]\ln\left(\frac{c}{c_o}\right)\right| \tag{5}$$

Applying Equation (5) to the endpoints of the error-bracketing lines in Figure 20 gives an estimate of the maximum slope of the relationship (assuming linearity) as well as an estimate of the ratio of the intensities of the CO_2 and D_2O peaks at T_o = T(outside, z = 0 μm) and T = T(inside, z = 2000 μm). Since the concentration of CO_2 is always small, the intensity ratios approximate the mole fraction of CO_2 in D_2O and can be substituted for the concentrations in Equation (5). Substituting these ratios, 0.124 and 0.210, and the respective temperatures, 30°C and 12°C, gives:

$$\left|S_T\right|_{\max} = \left|\left[\frac{1}{(12 - 30)}\right]\ln\left(\frac{0.210}{0.125}\right)\right| = 0.03 \tag{6}$$

Similar results are obtained from the uncertainty values in the other plots, providing a reasonable estimate of the minimum absolute value for S_T than can be measured in these experiments. In conclusion, the results of this study indicate that

$$-0.03 < S_T < 0.03 \qquad (7)$$

If the absolute magnitude of S_T is smaller than 0.03, it is unlikely that it could be measured using the experimental approach employed here.

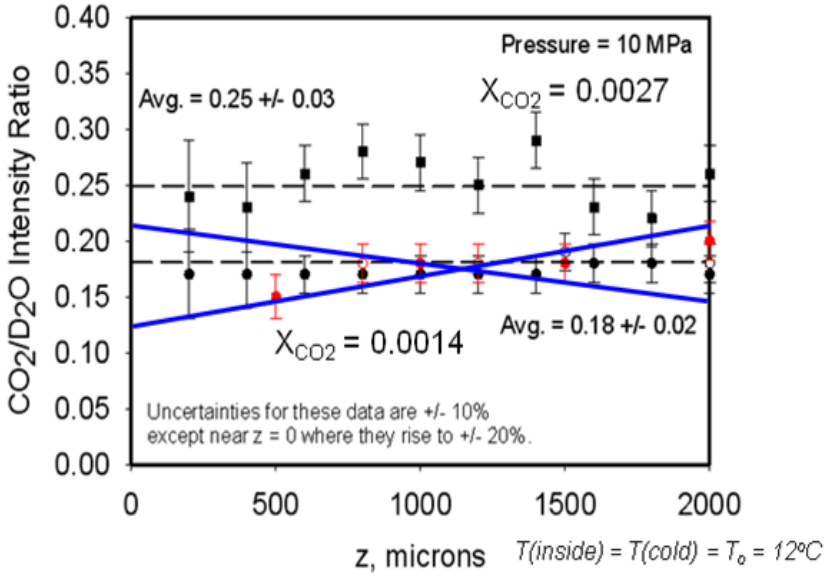

Figure 20. Re-plot of Figure 11 showing straight lines fitted by eye to limits of error bars of the data for $X(CO_2) = 0.0014$.

On the other hand, the results indicate that solutions of CO_2 dissolved in water do not exhibit S_T values as large as those determined for some other mixtures near their critical point of one of the components. Kempers (Kempers 2001) reported values of the thermal diffusion factor, α_T, significantly above 10 for mixtures of methane and propane above the critical point of methane. Given that α_T is related S_T in Equation (3) by $S_T \sim \alpha_T/T$ for dilute solutions, similar values of α_T in our experiments would have led to $|S_T| > 0.03$ (using an average temperature of 35°C). The sensitivity analysis performed above indicates that values of S_T of this magnitude should have been observable with the experimental approach used here. Consequently, it appears that solutions of CO_2 dissolved in water solutions do not exhibit the inordinately large Soret effect of other mixtures under conditions near the critical point of one of the components. This could be partly attributed to the low concentration of the "supercritical" component CO_2 compared to mixtures studied by Kempers where components were present at mole fractions exceeding 0.1.

4.2 Solutions of H_2O saturated with CO_2

Figures 17 and 18 seem to suggest the presence of a Soret effect in solutions of H_2O containing CO_2 above its solubility. The peak intensity parameter related to CO_2 is clearly smaller close to z = 0 μm (where T = 15°C) than it is near z = 2000 μm (where T = 11°C). The slope of the line connecting the two limiting positions is positive. However, it is important to remember that these experiments were conducted with excess CO_2 present. The H_2O phase was saturated with CO_2 at all temperatures and, since all temperatures were below the critical temperature of CO_2, the excess CO_2 was in the form of a

secondary liquid phase. For this reason, it seems more likely that the variation in Figures 16 and 17 is due to the relationship between solubility and temperature (i.e., position), rather than kinetic parameters. To check this possibility, we compared the fractional variation in concentration with temperature observed in this experiment with that expected from the variation in solubility.

Using the endpoints of the data in Figure 18, shown again in Figure 21, and substituting intensities for concentrations as discussed previously,

$$\frac{\Delta c / c_o}{\Delta T} = \frac{1}{T - T_o}\left(\frac{c - c_o}{c_o}\right) \approx \frac{1}{T - T_o}\left(\frac{I - I_o}{I_o}\right) = \frac{1}{11 - 15}\left(\frac{1 - 0.876}{1}\right)$$
$$\frac{\Delta c / c_o}{\Delta T} \approx -0.03 \pm 0.01\,^{o}C^{-1} \qquad (8)$$

Performing the same calculate using solubility data for CO_2 in H_2O at 10 MPa between 12°C and 15°C (Spycher 2002) gives

$$\frac{\Delta c / c_o}{\Delta T} = \frac{1}{T - T_o}\left(\frac{c - c_o}{c_o}\right) \approx \frac{1}{12 - 15}\left(\frac{0.001}{0.028}\right)$$
$$\frac{\Delta c / c_o}{\Delta T} \approx -0.01 \pm 0.01\,^{o}C^{-1} \qquad (9)$$

A good case is made from the above comparative calculations that the trend in CO_2 concentrations within the annulus, in the case of H_2O saturated with CO_2 and excess liquid CO_2 present, is a simple consequence of the variation in solubility of CO_2 as a function of temperature.

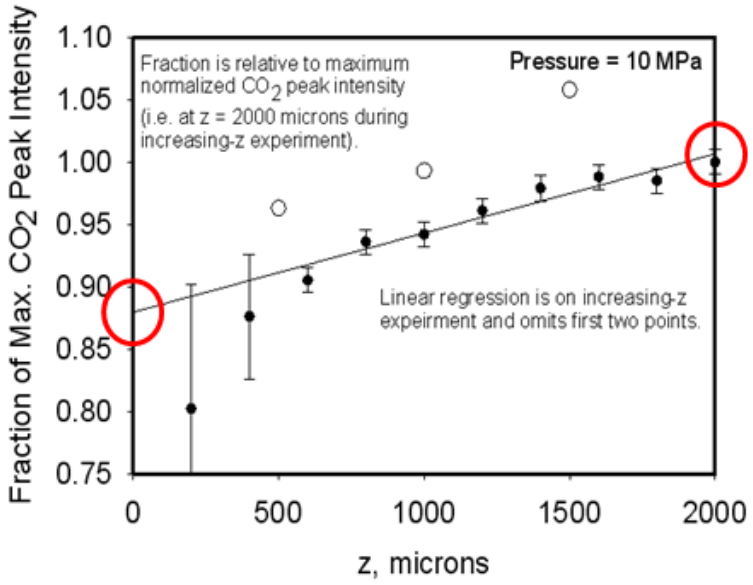

Figure 21. Re-plot of Figure 17 noting intensity values at z = 0 μm and z = 2000 μm that were used to compare the observed variation with temperature to predictions based on solubility.

4.2 Concentration calibration plots

The final calculations performed in this work concern the values of the relative Raman intensities measured over the course of several experiments with different mole fraction CO_2. Values of the intensity ratios (for the strongest peak of CO_2 to the D_2O or H_2O peak) were amassed and plotted versus the mole fraction of CO_2 in each mixture. Since minimal variation in concentration occurred within the annulus for experiments where a temperature gradient was applied, the ratios from both isothermal experiments and experiments with a temperature gradient were all used. The ratios were converted to the fraction of total intensity associated with CO_2 (to be slightly more quantitative relative to concentration) and results are shown in Figure 22.

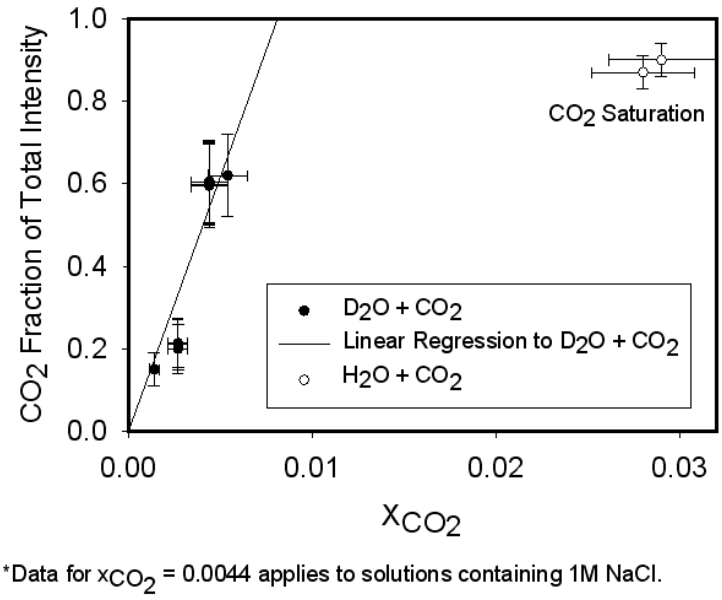

Figure 22. Plot of the fraction of total Raman scattering intensity attributed to CO_2 versus the mole fraction of CO_2 in the mixture as calculated from the quantities used in preparation.

As shown in Figure 22, the CO_2 intensity fraction scales linearly with the mole fraction of CO_2 for concentrations less than about 0.005. When the values for the CO_2-saturated solutions are included (at two temperatures), significant non-linearity is observed. The non-linearity is due to two factors. First, the CO_2-saturated solutions contained H_2O instead of D_2O and, consequently, the H-O-H bending mode instead of the D-O-D bending mode was used. Slight differences between the scattering cross sections for H_2O and D_2O may exist. Second, and most important, the CO_2 Fermi dyad has a significantly greater scattering cross section than the H-O-H bending mode. The impact of this difference is illustrated by calculations for the two extreme of CO_2 concentration as given below:

Low concentration of CO_2: $$\frac{c_{CO_2}}{c_{CO_2}+c_{H_2O}} \approx \frac{c_{CO_2}}{c_{H_2O}(\sim 1)} = \frac{s_{CO_2} I_{CO_2}}{s_{H_2O} I_{H_2O}} = const.\left(\frac{I_{CO_2}}{I_{H_2O}}\right)$$

High concentration of CO_2: $$\frac{s_{CO_2} I_{CO_2}}{s_{CO_2} I_{CO_2} + s_{H_2O} I_{H_2O}} \approx \frac{s_{CO_2} I_{CO_2}}{s_{CO_2} I_{CO_2}} = 1$$

At low CO_2 concentrations, the intensity ratio (or fraction) should scale directly with the concentration. At high CO_2 concentrations, the ratio will approach unity. Given the relative size of the scattering coefficients, $s_{CO2} >> s_{H2O}$, the transition to asymptotic behavior (curve approaching unity) should occur at relatively small CO_2 concentrations. In this case, the CO_2 bands come to dominate the spectra at mole fractions significantly below the saturation concentration.

The alternative calibration plot shown in Figure 23 corroborates the statements made above. In this figure, the measured intensity ratios were converted to ratios of the mole fractions (CO_2/D_2O) using the solubility of CO_2 in H_2O as a single calibration point (i.e., $X(CO_2) = 0.028$). The formula used for the conversion is shown in the figure, were f is the conversion factor determined from the CO_2 solubility. The converted intensities ratios were then plotted against the ratios of concentrations calculated from the amounts of CO_2 and D_2O (or H_2O) mixed during sample preparation. The resulting plot is near-linear as expected, with some small deviations near the origin attributed to difficulties in quantitative transfer of the gas to the pump, assurance of complete dissolution of the CO_2 in the water during mixing, and the presence of a systematic uncertainty in the pump volume.

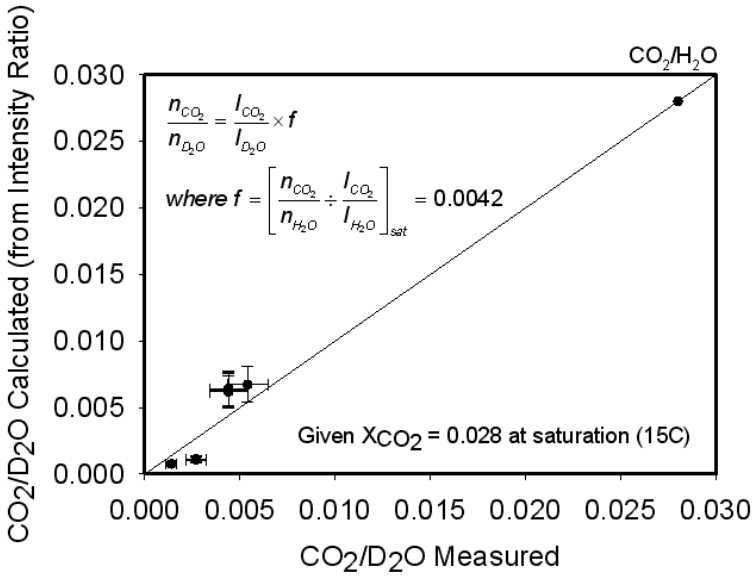

Figure 23. Plot of the fraction of total Raman scattering intensity attributed to CO_2 versus the mole fraction of CO_2 in the mixture as calculated from the quantities used in preparation.

5.0 References

Amirkhanov DG and AG Usmanov. 1987. "Thermal Diffusivity of Hydrocarbon in the Near-Critical Region." *Inzhenerno-Fizicheskii Zhurnal* 52(1):106-107.

Battestelli A, C Calore, and K Pruess. 1997. "The Simulator TOUGH2/EWASG for Modelling Geothermal Reservoirs with Brines and Non-Condensible Gas." *Geothermics* 26(4): 437-464. Available at http://dx.doi.org/10.1016/S0375-6505(97)00007-2.

Cabaco MI, M Besnard, S Longelin, and Y Danten. 2010a. "Evolution with the Density of CO_2 Clustering Studied by Raman Spectroscopy." *Journal of Molecular Liquids* 153(1):15-19. Available at http://dx.doi.org/10.1016/j.molliq.2009.09.007.

Cabaco MI and M Musso. 2010b. "Preface." *Journal of Molecular Liquids* 153(1):1. Available at http://dx.doi.org/10.1016/j.molliq.2010.03.013.

Cabaco MI, S Longelin, Y Danten, and M Besnard. 2007. "Local Density Enhancement in Supercritical Carbon Dioxide Studied by Raman Spectroscopy." *Journal of Physical Chemistry A* 111(50):12966. DOI: 10.1021/jp0756707.

Duhr S and D Braun. 2006. "Why Molecules Move Along a Temperature Gradient." *Proceedings of the National Academy of Sciences* 103(52):19678-19682. DOI: 10.1073/pnas.0603873103.

Horiba Jobin Yvon Raman Application Note. "Strain Measurements of a Si cap Layer Deposited on a SiGe Substrate Determination of Ge Content." *Semiconductor 01*. Available at http://www.horiba.com/fileadmin/uploads/Scientific/Documents/Raman/Semiconductors01.pdf

Kempers LJTM. 2001. "A Comprehensive Thermodynamic Theory of the Soret Effect in a Multicomponent Gas, Liquid, or Solid." *Journal of Chemical Physics* 115(14):6330. DOI: 10.1063/1.1398315.

Kolodner P, H Williams, and C Moe. 1988. "Optical Measurement of the Soret Coefficient of Ethanol/Water Solutions." *Journal of Chemical Physics* 88(10):6512. DOI:10.1063/1.454436.

Slavtchev S, G Simeonov, and S Van Vaerenbergh. 1999. "Technical Note: Marangoni Instability of a Layer of Binary Liquid in the Presence of Nonlinear Soret Effect." *International Journal of Heat and Mass Transfer* 42(15):3007-3011. Available at http://dx.doi.org/10.1016/S0017-9310(98)00353-6.

Koniger A, H Wunderlich, and W Kohler. 2010. "Measurement of Diffusion and Thermal Diffusion in Ternary Fluid Mixtures using a Two-Color Optical Beam Deflection Technique." *Journal of Chemical Physics* 132(17):174506. DOI: 10.1063/1.3421547.

Levenberg. 1944. "A Method for the Solution of Certain Non-Linear Problems in Least Squares." *The Quarterly of Applied Mathematics* 2: 164-168.

Nejad M, MZ Saghir, and MR Islam. 2001. “Role of Thermal Diffusion on Heat and Mass Transfer in Porous Media.” *International Journal of Computational Fluid Dynamics* 15:157. DOI:10.1080/10618560108970025.

Ning H and S Wiegand. 2006. “Experimental Investigation of the Soret Effect in Acetone/Water and Dimethylsulfoxide/Water Mixtures.” *Journal of Chemical Physics* 125(22):221102. DOI:10.1063/1.2402159.

Spycher N, K Pruess, and J Ennis-King. 2002, July. *CO_2-H_2O Mixtures in the Geological Sequestration of CO_2. I. Assessment and Calculation of Mutual Solubilities from 12 to 100°C and up to 600 bar*. LBNL-50991, Lawrence Berkeley National Laboratory, Berkeley, California.

Swinney HL and HZ Cummins. 1968. “Thermal Diffusivity of CO_2 in the Critical Region.” *Physical Review* 171(1):152-160. DOI:10.1103/PhysRev.171.152.

White MD and BP McGrail. 2002. “Numerical Investigations of Multifluid Hydrodynamics During Injection of Supercritical CO_2 into Porous Media.” In *Sixth International Conference on Greenhouse Gas Control Technologies*, pp. 449-455, ed. N Matsumiya, Research Institute of Innovative Technology for the Earth, October 1-4, 2002, Kyoto, Japan. http://dx.doi.org/10.1016/B978-008044276-1/50072-6.

Xu B, K Nagashima, JM DeSimone, and CS Johnson. 2003.“Diffusion of Water in Liquid and Supercritical Carbon Dioxide: An NMR Study.” *Journal of Physical Chemistry A* 107(1):1-3.

Zhang JL, XG Zhang, and BX Han. 2002. “Study on Intermolecular Interactions in Supercritical Fluids by Partial Molar Volume and Isothermal Compressibility.” *Journal of Supercritical Fluids* 22(1):15-19.

Pacific Northwest
NATIONAL LABORATORY

U.S. DEPARTMENT OF
ENERGY

Proudly Operated by Battelle *Since 1965*

902 Battelle Boulevard
P.O. Box 999
Richland, WA 99352
1-888-375-PNNL (7665)
www.pnl.gov